ROYAL SOCIETY OF CHEMISTRY

PAPER

Universal wetting transition of an evaporating water droplet on hydrophobic micro- and nano-structures†

Adrien Bussonnière,[ab] Masoud B. Bigdeli,[a] Di-Yen Chueh,[c] Qingxia Liu,[b] Peilin Chen[c] and Peichun Amy Tsai*[a]

Water-repellent, rough surfaces have a remarkable and beneficial wetting property: when a water droplet comes in contact with a small fraction of the solid, both liquid–solid adhesion and hydrodynamic drag are reduced. As a prominent example from nature, the lotus leaf—comprised of a wax-like material with micro- and nano-scaled roughness—has recently inspired numerous syntheses of superhydrophobic substrates. Due to the diverse applications of superhydrophobicity, much research has been devoted to the fabrication and investigations of hydrophobic micro-structures using established micro-fabrication techniques. However, wetting transitions remain relatively little explored. During evaporation, a water droplet undergoes a wetting transition from a (low-frictional) partial to (adhesive) complete contact with the solid, destroying the superhydrophobicity and the self-cleaning properties of the slippery surface. Here, we experimentally examine the wetting transition of a drying droplet on hydrophobic nano-structures, a previously unexplored regime. In addition, using a theoretical analysis we found a universal criterion of this wetting transition that is characterized by a critical contact angle. Different from previous results showing different critical droplet sizes, our results show a universal, geometrically-dependent, critical contact angle, which agrees well with various data for both hydrophobic micro- and nano-structures.

1 Introduction

Because of their promising applications for micro- and nano-fluidic devices,[1–5] condensation heat transfer systems,[6,7] friction control,[8–12] self-cleaning[13,14] and icephobic functionality,[15,16] there is currently significant interest in the wetting states on patterned hydrophobic substrates that form the so-called super-hydrophobic surfaces.[17,18] Despite these intriguing and useful applications, the large-scale implementation of superhydrophobic surfaces with robust non-wetting properties has remained challenging because an irreversible wetting transition can occur, destroying a gas-trapping state. For instance, various experiments, theoretical modeling, and numerical simulations have demonstrated that evaporation can naturally induce a wetting transition from an air-trapping Cassie–Baxter state (CB or the so-called "Fakir")[19,20] to a completely wetting Wenzel (W)[21] state on superhydrophobic substrates.[22–30]

Different techniques have been developed in response to prevent the transition to the complete wetting state. These methods vary from altering the geometrical and chemical properties of the surfaces[31–37] to stimulating substrates with light, heat, electric potential or mechanical vibration.[38–41] The fabrication of extremely robust superhydrophobic surfaces is still very active. An advantageous CB state, albeit metastable, may be achieved by tuning the aspect ratio and the packing density of the pillars.[22,24] Hence, finer textures at the nano-scale may be favorable for durable superhydrophobicity. Insofar, only a few studies have been performed to elucidate the influence of the nano-textured surfaces on the wetting behavior of an evaporating droplet.[31,36,42] This pioneering work used (hierarchical) nano-grass structures, and the critical conditions for the CB to Wenzel wetting transition using nano-structures have not been concluded.

In this paper, using both theory and experiment, we elucidate the evaporation dynamics, wetting state and transition of small droplets on regular nano-structures. Systematic measurements of the evaporation rate, droplet contact angle and radius, and critical transition points were conducted for various nano-patterns. Owing to the nano-structuring, for the first time, we were able

a Department of Mechanical Engineering, University of Alberta, Edmonton, AB, T6G 1H9, Canada. E-mail: peichun.amy.tsai@ualberta.ca; Fax: +1 780-492-2200; Tel: +1 780-492-5425

b Department of Chemical and Materials Engineering, University of Alberta, Edmonton, AB, T6G 1H9, Canada

c Applied Sciences, Academia Sinica, 128 Section 2, Academia Road, Nankang, Taipei 11529, Taiwan

† Electronic supplementary information (ESI) available: SEM images of nano-structures, non-spherical drop shapes, evaporation flux, error analysis of contact angle, and supporting movie. See DOI: 10.1039/c6sm02287a

This journal is © The Royal Society of Chemistry 2017

to investigate extremely dilute structures and high aspect ratio pillars. Our results highlight the interplay between the geometrical properties and the universality of the critical contact angle at the CB to W wetting transition for both hydrophobic micro- and nano-structured substrates.

2 Experimental

2.1 Sample preparation

To prepare nano-patterned silicon (Si) molds, the surfaces of the (100)-oriented Si wafers were cleaned by sonication in acetone and ethanol at room temperature for 10 and 5 min, respectively. The Si substrates were then placed in the boiling Piranha solution [H_2SO_4/H_2O_2, 4 : 1 (v/v)] and RCA solution [$NH_3/H_2O_2/H_2O$, 1 : 1 : 5 (v/v/v)] for 1 h each and then rinsed several times with deionized water. The cleaned Si wafers were spin-coated with a photoresist (TMHR ip3650, TOK) and then patterned using I-line projection photolithography (FPA-3000i5+ Stepper, Canon). The designed metal masks with 200 nm or 400 nm square array patterns and a periodicity P (ranging from 800 nm to 2 μm) were applied. After the development of the photoresist, Si micro/nanopillar arrays were formed through inductively coupled plasma dry etching (ICP; MESC Multiplex, STS) with 600 W power and 11.5 W bias power, when two working gases per duty cycle were used (25 sccm of SF6 for 7 s; 75 sccm of C4F8 for 7 s). The height of the Si micro/nanopillar arrays could be tuned by changing the etching time. The height of the nano-pillars, H, is 1 or 2 μm. The remaining photoresist was removed in boiling Piranha solution [H_2SO_4/H_2O_2, 4 : 1 (v/v)].

Finally, the nano-patterned Si wafers were diced, cleaned with Piranha, and hydrophobized using trichloro(1,1,2,2-perfluoocytl)-silane.

The superhydrophobic surfaces consist of nano-scale cylindrical pillars in a square lattice. We investigated a variety of nano-textures, by varying the periodicity P (from 0.8 to 2 μm), the post diameter D (200 and 400 nm) and the pillar height H (1 and 2 μm) (see the SEM images in Fig. 1a and Fig. S1, (ESI†)). The original silica surfaces were coated with a hydrophobic layer using trichloro(1,1,2,2-perflurocytl)-silane, leading to a contact angle of 115° on the smooth surface. The nano-structures were characterised with two crucial geometrical parameters: surface roughness $r = 1 + \dfrac{\pi DH}{P^2}$, the ratio of the actual to the apparent surface area, and the solid fraction $\Phi = \dfrac{\pi D^2}{4P^2}$, corresponding to the packing fraction of the nano-pillars. In other words, r describes the relative change in the liquid/solid area compared to a flat surface in a Wenzel state;[21] Φ quantifies the percentage of the liquid–solid contact area in a Cassie–Baxter case.[19] Our regular nano-patterned surfaces have a small packing fraction, $0.0079 \leq \Phi \leq 0.20$, and a wide range of roughness, $1.1 \leq r \leq 4.92$.

2.2 Experimental setup

Two synchronized cameras were used to record evaporation dynamics, one taking the side-view and the other top-view images at a rate of 0.5 frames per second. The side-view was magnified using a long-range microscope and the top-view
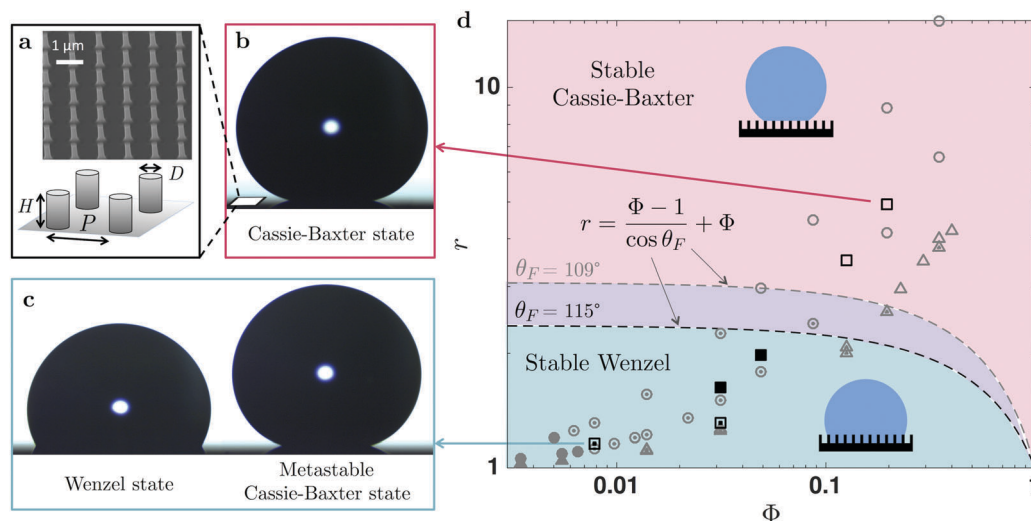

Fig. 1 Initial wetting state. (a) A scanning electron micrograph and a schematic representation of the hydrophobic nano-structures, whose geometric parameters are revealed by □, ▣, ■ in the phase space of surface roughness, r, and the packing fraction of nano-pillars, Φ, in (d). Using an energetic argument,[44] the phase space shown in (d) can be divided in a stable Cassie–Baxter (CB) state domain (in red) and a stable Wenzel state region (in blue). The previous experimental data by Barbieri et al.,[45] (○, ◉, ●) and Jung et al.,[23] (△, ▲, ▲) using microstructures are also plotted for a comparison. Due to the different contact angles on the smooth surfaces (θ_F), the CB–W separation lines are depicted differently: the lower one for our data using nanostructures ($\theta_F = 115° -$) compared to the previous studies ($\theta_F = 109° --$). For high roughness surfaces, the initial drop shape always exhibits superhydrophobic states (denoted by the open symbols □, ○, △); for instance, the initial droplet shown in (b), with $r = 4.92$ and $\Phi = 0.20$, has a contact angle higher than 165°, whereas at low roughness (e.g., in (c)) $r = 1.16$ and $\Phi = 0.0079$) a Wenzel state (denoted by the filled symbols, ●, ●, ▲) is more likely observed. However, by carefully depositing the drop, a metastable Cassie–Baxter state (▣, ◉, ▲) with a larger contact angle is also found (e.g., in (c) $r = 1.16$ and $\Phi = 0.0079$).

using a fixed focal length lens mounted on an extension tube. Top-view visualisation was used to check drop sphericity. Drop shapes were first extracted from the side-view images using ImageJ software. The drop volume, contact angle, and base radius were measured using an axisymmetric drop shape analysis (ADSA)[43] Matlab code by considering the gravity effect on the Laplace pressure. Instead of the spherical cap model, the ADSA method was used because non-spherical droplet shapes were observed, especially when the droplet size was comparable with the capillary length (see the ESI† for details). The experiments were conducted at 25 °C and 16% relative humidity (H_a).

3 Results and discussion

3.1 Wetting state

Fig. 1 summaries the initial wetting state of a water droplet (of 10 μL) on various hydrophobic nano-structures. Snapshots in Fig. 1(b) and (c) reveal representative initial drop shapes for two nano-structures ($r = 4.93$ and $r = 1.16$, respectively). We observed two distinct wetting behaviours of the initial water droplet on various hydrophobic nano-structures, manifested by two different apparent contact angles, θ_{app}. At contact angles $\theta_{app} > 160°$, the drop rests only on the top of the pillars, while air is trapped beneath. In this so-called Cassie–Baxter state,[19] the droplet has hybrid inter-facial gas–liquid and liquid–solid contacts. By contrast, the liquid could completely wet the entire structure forming a smaller $\theta_{app} \approx 120°$, in an impaled or Wenzel state,[21] with solely homogeneous liquid–solid contact. This difference in apparent contact angles arises from the change in the solid–liquid contact area. For a CB drop, the contact angle depends on the solid fraction Φ and is defined by $\cos\theta_{CB} = \Phi(\cos\theta_F + 1) - 1$, obtained with a surface energy argument.[19] In contrast, in the Wenzel state the wet area is characterised by the surface roughness r, and thus the apparent contact angle is given by $\cos\theta_W = r\cos\theta_F$, where θ_F is the contact angle measured on the flat surface of the same material.[21]

The impaled (Wenzel) state makes the surface sticky by increasing the retention forces[46] via an increase of the contact angle hysteresis[47,48] and contact radius, resulting in a loss of superhydrophobicity.[49] The stability of the CB state can be predicted theoretically by comparing the two surface energies.[44] The resulting criterion depends on the geometric parameters r and Φ in relation with θ_F, shown by the dashed line in Fig. 1. For given surface properties (θ_F), the Cassie–Baxter state will be favorable on patterned surfaces with a high roughness of $r > \dfrac{\Phi - 1}{\cos\theta_F} + \Phi$ (i.e., the red area in Fig. 1d). This prediction agrees well with our observations; we always observed a Cassie–Baxter state of the initial drop for greater r (e.g., $\theta_{app} \gtrsim 160°$ for $r = 3.51$ and $r = 4.92$). The Wenzel state is theoretically more favorable for low-roughness surfaces (the blue regime in Fig. 1d). Indeed, consistent with this prediction, we only observed an initial Wenzel drop in the intermediate range of roughness (e.g., $r = 1.63$ and $r = 1.98$).

For even lower roughness ($r = 1.16$ and $r = 1.31$), corresponding to the stable Wenzel regime (marked in blue in Fig. 1d),

if no precautions were taken during the drop deposition a Wenzel state was more likely to be observed. However, by using a needle and a slow approach we were able to deposit a Cassie–Baxter drop. This metastable CB state, also reported on other micro-structures,[23,24,49] is unstable and undergoes a transition to the Wenzel state during the evaporation of a water droplet. Below, we focus on the results of such wetting transition and drop morphology during evaporation.

3.2 Evaporation dynamics

Fig. 2 shows our results for the contact radius and angle evolutions of evaporating water droplets on nano-structures, for the two different initial states: air-trapping CB and complete wetting Wenzel state (denoted in red and blue, respectively in Fig. 2). We found that drops exhibit similar behaviours regardless of the nano-structures and initial wetting states. In general, at the early stage the contact line is pinned, while the contact angle decreases due to the decreasing volume and hence the height during evaporation. Once the contact angle reaches the receding contact angle ($\approx 155°$ for the Cassie–Baxter state and $\approx 90°$ for the Wenzel state), the contact radius starts decreasing, while maintaining a nearly constant contact angle. Finally, at the end of the evaporation, the contact radius and angle decrease simultaneously. These three sequential stages of evaporation dynamics are known as the constant contact radius (CCR), constant contact angle (CCA), and mixed mode (of CCR and CCA),[50,51] which have been observed during drop evaporation on flat[50,52] and micro-structured[53–55] surfaces. A CB droplet evaporates mostly in the CCA mode due to the small contact angle hysteresis. Whereas, for impaled drops, the CCR mode is longer, lasting for almost the entire evaporation in the intermediate roughness range.

A classical theory that models the evaporation rate of a sessile water drop is based on diffusive transport of saturated vapor along the top droplet surface to the ambient air[56] (see the ESI†). We compare in Fig. 3 our experimental results using hydrophobic nano-structures with the theoretical prediction (dashed line) without the consideration of roughness r. The comparative quantity is a dimensionless mass flux rate, $\dot{\mathcal{M}} = \dfrac{\dot{M}}{R_b D(c_S - c_\infty)}$, derived from the vapor-diffusion model, where R_b is the base radius, D is the water vapor diffusion coefficient in air, c_S is the saturated vapor concentration, and c_∞ is the vapor concentration at infinity (see the ESI† for the details). Regardless of the nano-patterned surfaces, experimental data collapse, corroborating the theory that the evaporation rate only depends on the contact angle. Nevertheless, the classical theory based on a pure diffusion process slightly overestimates the evaporation rates measured on nano-patterned surfaces. This observation is in agreement with a recent study showing that drops evaporate more slowly on superhydrophobic surfaces.[57] This discrepancy has been attributed to the evaporation cooling effect. At a high contact angle, the contact radius becomes small, limiting the heat flux between the substrate and drop. Consequently, the droplet becomes colder, which in
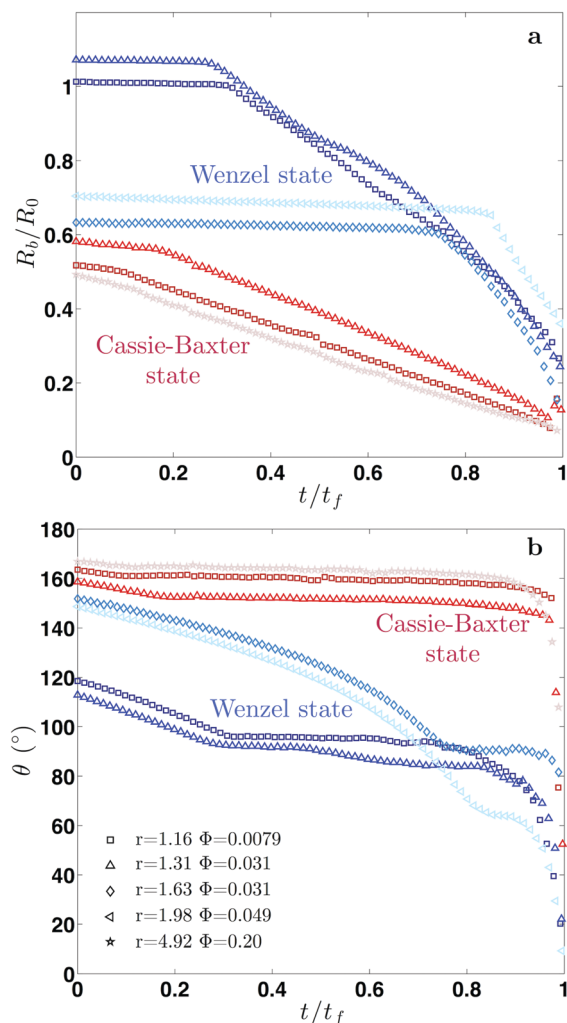
Fig. 2 Contact radius and angle dynamics during evaporation. (a) Evolution of the dimensionless base radius R_b/R_0, where R_0 is defined as the free drop radius of the same volume, and (b) contact angle dynamics in term of dimensionless time t/t_f, where t_f is the total evaporation time, for various surfaces and wetting states. The initial droplet of the Cassie–Baxter state is depicted by △, □ and ☆ (in red), whereas that of the Wenzel state by □, △, ◇ and ◁ (in blue). Initially, the drop evaporates with a constant contact radius (CCR mode). Subsequently, the contact radius decreases, while the contact angle remains constant (CCA mode). At the end of the evaporation, both the contact radius and angle decrease, corresponding to a mixed mode.

Fig. 3 Evaporation rate on hydrophobic nano-structures. Dimensionless outgoing mass flux rate, $\dot{\mathcal{M}}$, as a function of the contact angle, for different surfaces (see the ESI†). In spite of the different patterned structures, all the experimental data collapse, indicating that the evaporation rate mainly depends on the contact angle. Comparison with a vapor diffusion model derived by Popov[56] (dashed line) and an evaporation cooling correction[58] (solid line) reveals that the low evaporation rate observed can be attributed to a cooling effect.[58]

turn results in a decrease of saturated vapor concentration and hence a slower evaporation. Based on the numerical simulation of the temperature field during the evaporation, a correction factor has been introduced in the classical theory of droplet evaporation to account for the drop cooling.[58] Our experimental data show a better agreement with the latter model (see Fig. 3). For contact angles higher than $150°$, we noticed that the discrepancy increases significantly, and the experiments show a lower evaporation rate. This discrepancy may be attributed to the assumption of a spherical drop used by the theory[56,58] and the deviation of the drop shape from a spherical cap at such a high contact angle, observed in the experiments (see the ESI† note).
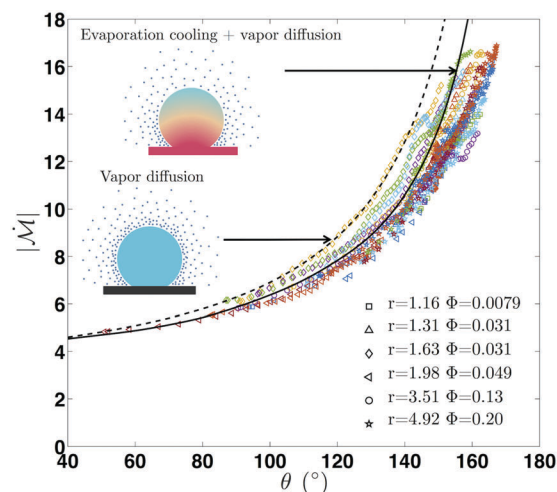
3.3 Cassie–Baxter to Wenzel wetting transition

For droplets initially in the CB state, sudden changes in the contact radius and contact angle are observed, while the droplet undergoes a transition to an impaled, *i.e.* complete wetting, state (see Fig. 4a). At this wetting transition, these changes arise due to liquid penetration into the nano-structures, thereby destroying superhydrophobicity. As a consequence, designing robust water repellant surfaces requires an insightful understanding of this wetting transition. A supporting movie illustrating the CB to W wetting transition corresponding to the data in Fig. 4 is provided (see the ESI† movie and info).

In previous studies, the transition is assumed to be triggered by the inter-pillar interface bending. As the drop evaporates, the Laplace pressure increases (as the drop curvature ($\propto 1/R$) increases), and this causes the bending of the air–liquid interface beneath the drop (between the solid pillars).[22,24,59] By denoting the maximum interface bending as δ, local curvature between two pillars scales as δ/l^2 with l being the inter-pillar spacing. Equating this curvature with the drop, one yields an estimation of the deformation $\delta \sim l^2/R$. The transition may take place if the liquid touches the structure bottom ($\delta = H$), or if the contact line starts to slide on pillar sides toward the bottom, *i.e.* if the local contact angle overcomes the advancing contact angle θ_a. Both scenarios lead to a critical drop radius: $R^\star \sim l^2/H$ for the "touch-down" and $R^\star \sim l/|\cos\theta_a|$ for the sliding model. Following these models, by using nano-patterned surfaces, we may be able to lower these critical radii to ≈ 4 μm and hence should extend the range of the superhydrophobic state to extremely small drops. However, our experimental critical radii were found to be between 100 and 500 μm (see Fig. 4a), different from the predictions using the above models.
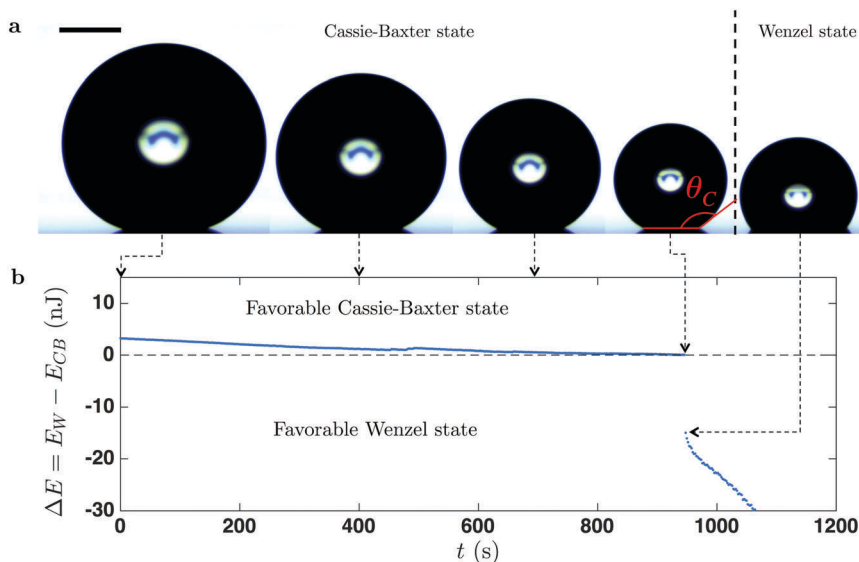
Fig. 4 Wetting transition. (a) Successive snapshots of an evaporating, metastable Cassie−Baxter drop on a superhydrophobic surface of a low roughness ($r = 1.16$). After 945 s, sudden changes in the contact radius and angle are observed corresponding to the wetting transition from a composite wetting CB to an impaled state. The scale bar in (a) corresponds to 500 μm. By comparing the surface energies of each states (b) using eqn (6) and (7), the critical transition, denoted by θ_C, occurs when both states have the same energy, i.e., $\Delta E = E_W - E_{CB} = 0$. Subsequently, the drop jumps to a Wenzel state that has a much lower surface energy.

Based on the surface energy calculation[26] as an alternative approach, we derived another criterion which is able to account for our own experimental results on nano-structures and the former results using micro-structures. We compared the surface energy of each (CB or Wenzel) state and accounted for the change in the contact angle during evaporation. According to this method, these surface energies at the Cassie–Baxter (CB) and Wenzel (W) states are expressed as:

$$E_{CB} = S_b(\gamma_{gs}r + \gamma(1 - \Phi(1 + \cos\theta))) + \gamma S_c, \qquad (1)$$

$$E_W = S_b(\gamma_{gs}r - \gamma r \cos\theta) + \gamma S_c, \qquad (2)$$

where S_b is the base surface area, S_c is the surface of the spherical cap, γ_{lg}, γ_{gs} and γ are the surface tension of the liquid–solid, gas–solid and gas–liquid interfaces, respectively.[26] The detailed derivation can be found in the Appendix.

Fig. 4b shows the evolution over time of the difference between Wenzel and Cassie energies, $\Delta E = E_W - E_{CB}$, for the surface with $r = 1.16$. At the beginning of the evaporation, the surface energy of a Cassie–Baxter drop is lower and thus stable; indeed, we observed a higher contact angle while the drop sits on the pillar top. During the evaporation, E_{CB} decrease slightly faster than the Wenzel one, E_W, resulting in a decrease of the energy difference. Subsequently, when the Cassie–Baxter and Wenzel states have the same energy ($\Delta E = E_W - E_{CB} = 0$), the wetting transition takes place (e.g., after 945 s in Fig. 4b). The proposed model is able to predict the transition for hydrophobic nano-structures, while the two aforementioned models significantly under-predict the critical value, suggesting the universal character of this approach. To validate this universality, we compare our theoretical results with various experimental findings, using a variety of geometric parameters for

micro-structures. To this end, we first derive a simple criterion based on the surface energy model. As shown in Fig. 4b, the wetting transition occurs at the critical contact angle θ_C when $\Delta E = 0$, which can be expressed as: $-r\cos\theta_C = 1 - \Phi(1 + \cos\theta_C)$ by setting $E_W = E_{CB}$. Consequently, the criterion for the CB to Wenzel transition is

$$\cos\theta_C = \frac{\Phi - 1}{r - \Phi}, \qquad (3)$$

implying that the wetting transition happens at a critical contact angle that universally depends on the geometric parameters of the micro- or nano-patterns.

We now compare, in Fig. 5, this criterion with our experiments using nano-structures (◊) and ten other studies found in the literature using a wide variety of micro-patterned substrates. Regardless of the structure or the material, our critical condition is in good agreement with experimental data, demonstrating its universality. The surface energy calculation is a first-order approximation without considering the energy associated with the (pinned) contact line, and thus a small deviation of the various experimental data from the prediction exists. Several factors can also contribute to this discrepancy: imperfect (square or cylindrical) pillar shapes, pinned contact lines, small chemical contamination, different models used for calculating the contact angle, and the measurement uncertainty stems from the contact radius or/and droplet height. We carried out error analysis and noticed that a 10% measurement uncertainty in the contact radius and droplet height (of ≈20 μm) can contribute to a ≈8% error in the contact angle.

It is interesting to note that while previous models predicted a critical contact radius, our approach leads to a critical contact angle reflecting the difference in the underlying mechanism
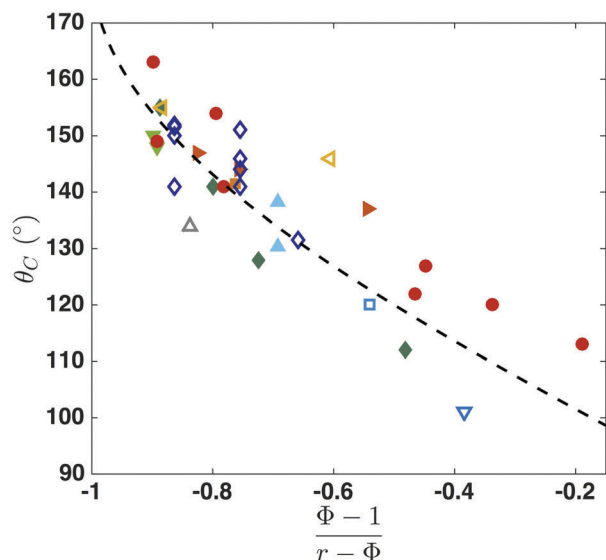
Fig. 5 Universal criterion of the critical contact angle at the Cassie–Baxter to Wenzel wetting transition. Comparison between the critical contact angle derived in this paper (dashed line) with our experimental data (◇) and the results reported by Blanco-Gomez et al.[60] (■), Chuang et al.[61] (□), Dicuangco et al.[28] (△), Dubov et al.[25] (◆), Jung et al.[59] (▼), McHale et al.[53] (▲), Tsai et al.[26] (▽), Wang et al.[62] (▶), Xu et al.[55] (◁) and Jung et al.[23] (●). Our criterion is in good agreement with experimental data regardless of the patterns and hydrophobic materials, demonstrating the universality of the criterion for the critical CB to Wenzel wetting transition.

triggering the wetting transition. Some data using microstructures of $P > 50$ μm in Fig. 5 are consistent with the predictions by the touch-down/sliding criteria as well as our model, implying that both mechanisms may play a role in triggering the CB to W transition. However, for nanostructures and some microstructures of smaller $P < 50$ μm[23,25,26] the touch-down/sliding model appears to underestimate the transition. We think that for smaller pillars, contact line pinning and imperfectly shaped pillars likely play a significant role, and these influences should be taken into account and remain an open question.

This new criterion, moreover, revises the way of maintaining a metastable CB state. Previous studies suggest that a reduction of the inter-pillar spacing would extend the CB state to small drops (via $R^\star \sim l^2/H$ or $l/|\cos\theta_a|$); however, these predictions were not observed for nano-patterned pillars. In contrast, for extending the gas-trapping CB state, our new finding suggests a minimisation of θ_C, and hence $|(\Phi - 1)/(r - \Phi)|$, by exploiting eqn (3).

4 Conclusions

In summary, for the first time we carried out systematic sets of theoretical and experimental examinations of the dynamic wetting transition from a Cassie–Baxter to a Wenzel state during drop evaporation on nano-structured surfaces. Surprisingly, the downscaling of structures to the nanoscale does not sustain the stability of superhydrophobicity, which was expected by previous analyses. We extended a previous model using the surface energy to derive a new and universal criterion that is able to account

for our experimental results (using nano-structures) and various data (with micro-structures) in the literature. From this unifying criterion, we see that the CB to Wenzel transition can occur even at a high contact angle ($\approx 150°$) for hydrophobic structures with both low roughness and solid fraction. In contrast, the transition to an impalement state is expected at a lower contact angle ($\approx 100°$) when the roughness and/or the solid fraction increases. Consequently, increasing roughness is a powerful way to extend the CB state of water drops on hydrophobic micro/nano-structures during evaporation.

Appendix

The surface energy associated with the Cassie–Baxter state on a patterned surface can be expressed as:

$$E_{CB} = \gamma_{sl}N\frac{\pi D^2}{4} + \gamma_{sg}N\left(\pi DH + P^2 - \frac{\pi D^2}{4}\right) + \gamma N\left(P^2 - \frac{\pi D^2}{4}\right) + \gamma S_c, \quad (4)$$

where H is the pillar height, D is the pillar diameter, P is the lattice periodicity, $N = \frac{\pi B^2}{4P^2} = \frac{S_b}{P^2}$ is the number of asperities under the drop, S_c is the surface of the spherical cap, S_b is the base surface and γ_{sl}, γ_{sg} and γ are the surface tension of the solid–liquid, solid–gas and liquid–gas interfaces, respectively. Using the definition of N, the surface energy for a Cassie–Baxter droplet on hydrophobic nano-structures, E_{CB}, can be calculated using the roughness r and the solid fraction Φ:

$$E_{CB} = S_b(\gamma_{sl}\Phi + \gamma_{sg}(r - \Phi) + \gamma(1 - \Phi)) + \gamma S_c, \quad (5)$$

and E_W, the surface energy of a Wenzel droplet is given by the following equation:

$$E_W = N\gamma_{sl}(\pi DH + P^2) + \gamma S_c = S_b\gamma_{sl}r + \gamma S_c. \quad (6)$$

The contact angle θ varies during evaporation, implying the change in the relationship between surface tensions. We use the Young–Dupré equation,[63] $\gamma_{sl} = \gamma_{sg} - \gamma\cos\theta$, by assuming (quasi-)force equilibrium in the horizontal direction during slow evaporation, and simply the surface energies for the two states in the following equations:

$$E_{CB} = S_b(\gamma_{gs}r + \gamma(1 - \Phi(1 + \cos\theta))) + \gamma S_c, \quad (7)$$

$$E_W = S_b(\gamma_{gs}r - \gamma r\cos\theta) + \gamma S_c. \quad (8)$$

References

1 L. Ionov, N. Houbenov, A. Sidorenko, M. Stamm and S. Minko, Adv. Funct. Mater., 2006, 16, 1153–1160.

2 D. Byun, J. Kim, H. S. Ko and H. C. Park, Phys. Fluids, 2008, 20, 113601.

3 P. Tsai, A. M. Peters, C. Pirat, M. Wessling, R. G. Lammertink and D. Lohse, Phys. Fluids, 2009, 21, 112002.

4 L. Bocquet and P. Tabeling, Lab Chip, 2014, 14, 3143–3158.

5 J. Lee, T. Laoui and R. Karnik, *Nat. Nanotechnol.*, 2014, **9**, 317–323.

6 J. Rafiee, X. Mi, H. Gullapalli, A. V. Thomas, F. Yavari, Y. Shi, P. M. Ajayan and N. A. Koratkar, *Nat. Mater.*, 2012, **11**, 217–222.

7 N. Miljkovic and E. N. Wang, *MRS Bull.*, 2013, **38**, 397–406.

8 C. H. Choi, U. Ulmanella, J. Kim, C. M. Ho and C. J. Kim, *Phys. Fluids*, 2006, **18**, 087105.

9 A. Steinberger, C. Cottin-Bizonne, P. Kleimann and E. Charlaix, *Nat. Mater.*, 2007, **6**, 665–668.

10 L. Bocquet and E. Lauga, *Nat. Mater.*, 2011, **10**, 334–337.

11 E. Karatay, A. S. Haase, C. W. Visser, C. Sun, D. Lohse, P. A. Tsai and R. G. Lammertink, *Proc. Natl. Acad. Sci. U. S. A.*, 2013, **110**, 8422–8426.

12 J. P. Rothstein, *Annu. Rev. Fluid Mech.*, 2010, **42**, 89–109.

13 R. Blossey, *Nat. Mater.*, 2003, **2**, 301–306.

14 K. Liu and L. Jiang, *Annu. Rev. Mater. Res.*, 2012, **42**, 231–263.

15 P. Guo, Y. Zheng, M. Wen, C. Song, Y. Lin and L. Jiang, *Adv. Mater.*, 2012, **24**, 2642–2648.

16 V. Hejazi, K. Sobolev and M. Nosonovsky, *Sci. Rep.*, 2013, **3**, 2194.

17 J. Bico, U. Thiele and D. Quéré, *Colloids Surf., A*, 2002, **206**, 41–46.

18 B. Bhushan and Y. C. Jung, *Prog. Mater. Sci.*, 2011, **56**, 1–108.

19 B. D. Cassie and S. Baxter, *J. Chem. Soc., Faraday Trans.*, 1944, **40**, 546–551.

20 D. Quéré, *Rep. Prog. Phys.*, 2005, **68**, 2495–2532.

21 R. N. Wenzel, *Ind. Eng. Chem. Res.*, 1936, **28**, 988–994.

22 S. Moulinet and D. Bartolo, *Eur. Phys. J. E: Soft Matter Biol. Phys.*, 2007, **24**, 251–260.

23 Y. C. Jung and B. Bhushan, *J. Microsc.*, 2008, **229**, 127–140.

24 M. Reyssat, J. M. Yeomans and D. Quéré, *EPL*, 2008, **81**, 26006.

25 A. Dubov, K. Perez Toralla, A. Letailleur, E. Barthel and J. Teisseire, *J. Micromech. Microeng.*, 2013, **23**, 125013.

26 P. Tsai, R. G. H. Lammertink, M. Wessling and D. Lohse, *Phys. Rev. Lett.*, 2010, **104**, 2–3.

27 H. C. Fernandes, M. H. Vainstein and C. Brito, *Langmuir*, 2015, **31**, 7652–7659.

28 M. Dicuangco, S. Dash, J. A. Weibel and S. V. Garimella, *Appl. Phys. Lett.*, 2014, **104**, 201604.

29 D. Murakami, H. Jinnai and A. Takahara, *Langmuir*, 2014, **30**, 2061–2067.

30 P. Papadopoulos, L. Mammen, X. Deng, D. Vollmer and H. J. Butt, *Proc. Natl. Acad. Sci. U. S. A.*, 2013, **110**, 3254–3258.

31 U. Tuvshindorj, A. Yildirim, F. E. Ozturk and M. Bayindir, *ACS Appl. Mater. Interfaces*, 2014, **6**, 9680–9688.

32 G. Whyman and E. Bormashenko, *Langmuir*, 2011, **27**, 8171–8176.

33 X. Liu, Q. Ye, X. Song, Y. Zhu, X. Cao, Y. Liang and F. Zhou, *Soft Matter*, 2011, **7**, 515–523.

34 K. C. Park, H. J. Choi, C. H. Chang, R. E. Cohen, G. H. McKinley and G. Barbastathis, *ACS Nano*, 2012, **6**, 3789–3799.

35 L. Schneider, M. Laustsen, N. Mandsberg and R. Taboryski, *Sci. Rep.*, 2016, **6**, 21400.

36 C. H. Choi and C. J. Kim, *Langmuir*, 2009, **25**, 7561–7567.

37 Y. Liu, Z. Lin, W. Lin, K. S. Moon and C. Wong, *ACS Appl. Mater. Interfaces*, 2012, **4**, 3959–3964.

38 W. Sun, S. Zhou, B. You and L. Wu, *J. Mater. Chem. A*, 2013, **1**, 3146–3154.

39 H. S. Lim, D. Kwak, D. Y. Lee, S. G. Lee and K. Cho, *J. Am. Chem. Soc.*, 2007, **129**, 4128–4129.

40 L. Xu, W. Chen, A. Mulchandani and Y. Yan, *Angew. Chem., Int. Ed.*, 2005, **44**, 6009–6012.

41 J. B. Boreyko and C. H. Chen, *Phys. Rev. Lett.*, 2009, **103**, 174502.

42 B. Bhushan, K. Koch and Y. C. Jung, *Soft Matter*, 2008, **4**, 1799–1804.

43 O. Río and A. Neumann, *J. Colloid Interface Sci.*, 1997, **196**, 136–147.

44 J. Bico, C. Tordeux and D. Quéré, *EPL*, 2001, **55**, 214–220.

45 L. Barbieri, E. Wagner and P. Hoffmann, *Langmuir*, 2007, **23**, 1723–1734.

46 C. G. L. Furmidge, *J. Colloid Sci.*, 1962, **17**, 309–324.

47 G. McHale, N. J. Shirtcliffe and M. I. Newton, *Langmuir*, 2004, **20**, 10146–10149.

48 B. Bhushan, M. Nosonovsky and Y. C. Jung, *J. R. Soc., Interface*, 2007, **4**, 643–648.

49 A. Lafuma and D. Quéré, *Nat. Mater.*, 2003, **2**, 457–460.

50 R. G. Picknett and R. Bexon, *J. Colloid Interface Sci.*, 1977, **61**, 336–350.

51 H. Y. Erbil, *Adv. Colloid Interface Sci.*, 2012, **170**, 67–86.

52 J. H. Kim, S. I. Ahn, J. H. Kim and W. C. Zin, *Langmuir*, 2007, **23**, 6163–6169.

53 G. McHale, S. Aqil, N. J. Shirtcliffe, M. I. Newton and H. Y. Erbil, *Langmuir*, 2005, **21**, 11053–11060.

54 K. R. Khedir, G. K. Kannarpady, H. Ishihara, J. Woo, S. Trigwell, C. Ryerson and A. S. Biris, *J. Phys. Chem. C*, 2011, **115**, 13804–13812.

55 W. Xu, R. Leeladhar, Y. T. Kang and C. H. Choi, *Langmuir*, 2013, **29**, 6032–6041.

56 Y. O. Popov, *Phys. Rev. E: Stat., Nonlinear, Soft Matter Phys.*, 2005, **71**, 1–17.

57 S. Dash and S. V. Garimella, *Langmuir*, 2013, **29**, 10785–10795.

58 Z. Pan, J. Weibel and S. Garimella, *Langmuir*, 2014, **30**, 9726–9730.

59 Y. C. Jung and B. Bhushan, *Scr. Mater.*, 2007, **57**, 1057–1060.

60 G. Blanco Gomez, A. Glidle, L. M. Flendrig and J. M. Cooper, *Microelectron. Eng.*, 2009, **86**, 1325–1328.

61 Y. C. Chuang, C. K. Chu, S. Y. Lin and L. J. Chen, *Soft Matter*, 2014, **10**, 3394–3403.

62 G. Wang, Z. H. Jia and H. N. Yang, *Colloid Polym. Sci.*, 2016, **294**, 851–858.

63 P. G. de Gennes, *Rev. Mod. Phys.*, 1985, **57**, 827–863.